International Journal of Solids and Structures 135 (2018) 26–36

Contents lists available at ScienceDirect

International Journal of Solids and Structures

journal homepage: www.elsevier.com/locate/ijsolstr

# Probability that a band-gap extremum is located on the irreducible Brillouin-zone contour for the 17 different plane crystallographic lattices

Florian Maurin[a,b,*], Claus Claeys[a,b], Elke Deckers[a,b], Wim Desmet[a,b]

[a] KU Leuven, Department of Mechanical Engineering, Division PMA Celestijnenlaan 300, Leuven B-3001, Belgium
[b] Flanders Make, Belgium

ARTICLE INFO

*Article history:*
Received 19 July 2017
Revised 25 October 2017
Available online 6 November 2017

*Keywords:*
Bloch theorem
Irreducible Brillouin zone
Plane crystallographic group
Band-gap
Dispersion
Porous phononic crystal

ABSTRACT

After recalling the first Brillouin zone (BZ) and the first irreducible Brillouin zone (IBZ) of a lattice in terms of its plane crystallographic group, we investigate the danger of restricting a band-gap detection to the contour of the IBZ, instead of its full IBZ. Based on hundreds of porous phononic crystal simulations, we provide for the 17 plane crystallographic groups (i) statistics of the band-gap localizations, (ii) probabilities to get non-full band-gaps, and (iii) averages of the bandwidth error made when only the IBZ contour is considered. It is found that for phononic crystals, the IBZ contour provides accurate results only for highly symmetric lattices.



## 1. Introduction

For time independent harmonic systems, the properties of a wave propagating along an axis do not depend on its sense (Brillouin, 1946). For this reason, the irreducible Brillouin zone (IBZ) is half of the Brillouin zone (BZ), and can be even reduced when the unit cell possesses some internal symmetries. For instance, for a square or a hexagonal unit cell with its bisectors and diagonals mirror symmetric, the first IBZ is reduced to a triangle covering an eighth or a twelfth of the first BZ, respectively (Kittel, 2007). These two crystallographic groups (*p4mm* and *p6mm*) are the most common ones in literature, and the first IBZ is most of the time correctly addressed (see for instance Phani et al., 2006). However, for periodic structures with symmetries of lower order, the first IBZ differs from these two previous examples and is often wrongly addressed, as attested by a literature review over the past decade presented in Table 1.

The reason of this misunderstanding could be that the theory for the plane crystallographic group (Cracknell, 1974) and the space group (Shmueli, 2008) is addressed to group theory experts, while massive developments of non-symmetric structures are driven by the potentials of metamaterials, and are often covered by non-physicists (e.g. engineers). It is our first goal in Section 2 to recall the strategy to identify the plane crystallographic group of a given lattice and then, provide the first BZ and IBZ for each plane crystallographic group (since only the first BZ and IBZ are considered in this manuscript, the term “first” is removed next for a sake of brevity). Note that for quasi-one and quasi-two dimensional waves propagating in two and three-dimensional glide or screw symmetric structures, a reduction of the unit cell size is also possible. Indeed, one can take advantage of the glide or the screw periods, instead of the (longer) translational periodicity (Maurin, 2016; Maurin et al., 2017).

In Section 3, the localization of the band-gap extrema is investigated with respect to the IBZ. Indeed, the band-gap detection is often restricted to the IBZ contour, whereas some counterexamples exist for non-symmetric periodic lattices (Nojima and Kamakura, 2008; Harrison et al., 2007; Farzbod and Leamy, 2011) and for lattices with a mirror reflection (Harrison et al., 2007; Gorshkov et al., 2017). Some additional cases that exhibit similar band-gap properties but for which the symmetry order of the lattice is higher are provided in this manuscript. Moreover, examples are also provided for which band-gaps observed on the IBZ contour are not full (no omnidirectional band-gap).

Finally, hundreds of different porous phononic crystals (plane strain aluminum with periodic vacuum holes) are simulated, and for each plane crystallographic group, we provide statistics of the band-gap localization, probabilities that a band-gap detected on

* Corresponding author at : KU Leuven, Department of Mechanical Engineering, Division PMA Celestijnenlaan 300, B-3001 Leuven, Belgium.
*E-mail address:* florian.maurin@kuleuven.be (F. Maurin).

https://doi.org/10.1016/j.ijsolstr.2017.11.006
0020-7683/

**Table 1**
Some references using the IBZ, ranked according to the plane crystallographic group (PCG) of the investigated lattice. See Section 2 for the nomenclature. By misdefined, it is meant that what is stated as the IBZ is not correct, but this might have no influence on the results. Note that in Bigoni et al. (2013), Zhao and Wang (2016), Bacigalupo and Gambarotta (2016), Baravelli and Ruzzene (2013), C.-L.Yang et al. (2017), Zhu et al. (2014), Spadoni et al. (2009b) and Tallarico et al. (2017), the definition of the IBZ (the area) is wrong, but its contour is correct.

| PCG | IBZ correctly addressed | IBZ misdefined |
|---|---|---|
| *p1* | H.-W.Dong et al. (2014), Nojima and Kamakura (2008), Meng et al. (2017), Shim et al. (2015), Harrison et al. (2007) | Gao et al. (2016) |
| *p2* | | Wang et al. (2015), Liu2017a |
| *p4* | Wang et al. (2014) | Bigoni et al. (2013), Zhao and Wang (2016), Bacigalupo and Gambarotta (2016), Baravelli and Ruzzene (2013), C.-L.Yang et al. (2017), Liu et al. (2017) |
| *p1m1* | Lardeau et al. (2016), Harrison et al. (2007) | Liu et al. (2009) |
| *p1g1* | | |
| *p2mm* | Spadoni et al. (2009a), Andreassen et al. (2015), Chen and Elbanna (2016), Wang et al. (2016b), Piccolroaz et al. (2017) | |
| *p2mg* | Chen and Elbanna (2016) | |
| *p2gg* | Shim et al. (2015) | |
| *c1m1* | Gonella and Ruzzene (2008), Gorshkov et al. (2017), Ahmed et al. (2017) | Claeys et al. (2016), Wang et al. (2016a), H.-W.Dong et al. (2014) |
| *c2mm* | Zhu and Deng (2016), Celli and Gonella (2015), Casadei and Rimoli (2013) | Wang et al. (2014) |
| *p3* | | Zhu et al. (2014), Tallarico et al. (2017) |
| *p6* | Liu et al. (2011) | Reda et al. (2017), Bacigalupo and Gambarotta (2016), Spadoni et al. (2009b) |
| *p4mm* | H.-W.Dong et al. (2014), Zhao and Wang (2016), Trainiti et al. (2016), Wang et al. (2014), Zhu and Deng (2016), Craster et al. (2012), Hladky-Hennion et al. (2008), Palermo and Marzani (2016), Hedayatrasa et al. (2016), Huang et al. (2017), Li et al. (2015); Liu et al. (2009), Miniaci et al. (2016), Collet et al. (2011), Meng et al. (2017), Bacigalupo and Gambarotta (2016), Phani et al. (2006) | |
| *p4gm* | Trainiti et al. (2016), Reda et al. (2017), Shim et al. (2015) | |
| *p3m1* | Schaeffer and Ruzzene (2015), Tallarico et al. (2017) | Wang et al. (2016a) |
| *p31m* | | |
| *p6mm* | Gorshkov et al. (2017), Yilmaz et al. (2007), Phani et al. (2006), Casadei and Rimoli (2013), Meng et al. (2017), Bacigalupo and Gambarotta (2016) | |

the IBZ contour is not full, and estimates of the bandwidth error when the band-gap detection is restricted to the IBZ contour. Conclusions follow.

## 2. Irreducible Brillouin zone in terms of the plane crystallographic group

Wave propagation in quasi-two-dimensional periodic structures is investigated with the Bloch theorem, restricting the analysis to a single unit cell, and taking advantage of periodic boundary conditions (Brillouin, 1946). We denote $\boldsymbol{r}_P$ the position of the point $P$ within the reference cell, and by $\boldsymbol{\rho}_P = \boldsymbol{r}_P + n_1\boldsymbol{e}_1 + n_2\boldsymbol{e}_2$ the same position $P$ relative to the $\{n_1\, n_2\}$th unit cell, where $\boldsymbol{e}_1$ and $\boldsymbol{e}_2$ are the basis vectors of the direct lattice. The reciprocal basis vectors are denoted $e^i$ $(i = 1, 2)$ and are given by $\boldsymbol{e}_i\boldsymbol{e}^j = \delta_{ij}$. Assuming a harmonic wave with angular frequency $\omega$ and amplitude $\hat{\boldsymbol{u}}$, the wave displacement $\boldsymbol{u}(\boldsymbol{r}_P, t)$ at time $t$ and position $\boldsymbol{r}_P$ is given by

$$\boldsymbol{u}(\boldsymbol{r}_P, t) = \hat{\boldsymbol{u}} e^{\boldsymbol{k}\cdot\boldsymbol{r}_P - \mathrm{i}\omega t}, \tag{1}$$

where $\mathrm{i}^2 = -1$, $\boldsymbol{k} = \mu_1\boldsymbol{e}^1 + \mu_2\boldsymbol{e}^2$ is the wave vector, and $\mu_1 = \boldsymbol{k}\cdot\boldsymbol{e}_1$ and $\mu_2 = \boldsymbol{k}\cdot\boldsymbol{e}_2$ are the complex propagation constant components. The wave at the point $\boldsymbol{\rho}_P$ yields

$$\boldsymbol{u}(\boldsymbol{\rho}_P, t) = \boldsymbol{u}(\boldsymbol{r}_P, t) e^{n_1\mu_1 + n_2\mu_2}. \tag{2}$$

The unit cells are parallelograms which can take 5 different shapes (the 5 two-dimensional Bravais lattices), namely oblique, rectangular, rhombic, square, and hexagonal (Kittel, 2007). The direct and reciprocal vectors for each cell are given in Table 2 and are illustrated in Fig. 1. Instead of representing the BZ by a parallelogram, one should use a hexagon, as shown in Fig. 1. The hexagonal representation of the BZ is preferred to the parallelogram one, since the longest possible wave-length can be used when all the directions are considered (Brillouin, 1946). Note that rectangles and squares are particular hexagons for which two opposite sides have a length null.

**Table 2**
Direct and reciprocal basis vectors for the 5 Bravais lattices.

| | $e_1$ | $e_2$ | $e^1$ | $e^2$ |
|---|---|---|---|---|
| Obl. | $a(1, 0)$ | $b(\cos\theta, \sin\theta)$ | $\frac{1}{a}(1, -\tan^{-1}\theta)$ | $\frac{1}{b}(0, \sin^{-1}\theta)$ |
| Rec. | $a(1, 0)$ | $b(0, 1)$ | $\frac{1}{a}(1, 0)$ | $\frac{1}{b}(0, 1)$ |
| Rho. | $a(1, 0)$ | $a(\cos\theta, \sin\theta)$ | $\frac{1}{a}(1, -\tan^{-1}\theta)$ | $\frac{1}{a}(0, \sin^{-1}\theta)$ |
| Squ. | $a(1, 0)$ | $a(0, 1)$ | $\frac{1}{a}(1, 0)$ | $\frac{1}{a}(0, 1)$ |
| Hex. | $a(1, 0)$ | $a(\frac{1}{2}, \frac{\sqrt{3}}{2})$ | $\frac{1}{a}(1, -\frac{1}{\sqrt{3}})$ | $\frac{1}{a}(0, \frac{2}{\sqrt{3}})$ |

In addition to its various shapes, a unit cell can possess additional rotational, glide and mirror reflection symmetries, forming the 17 different plane crystallographic groups, also called the plane symmetry groups or the wallpaper groups (see Fig. 2). But before its description, another group is introduced: the point group.

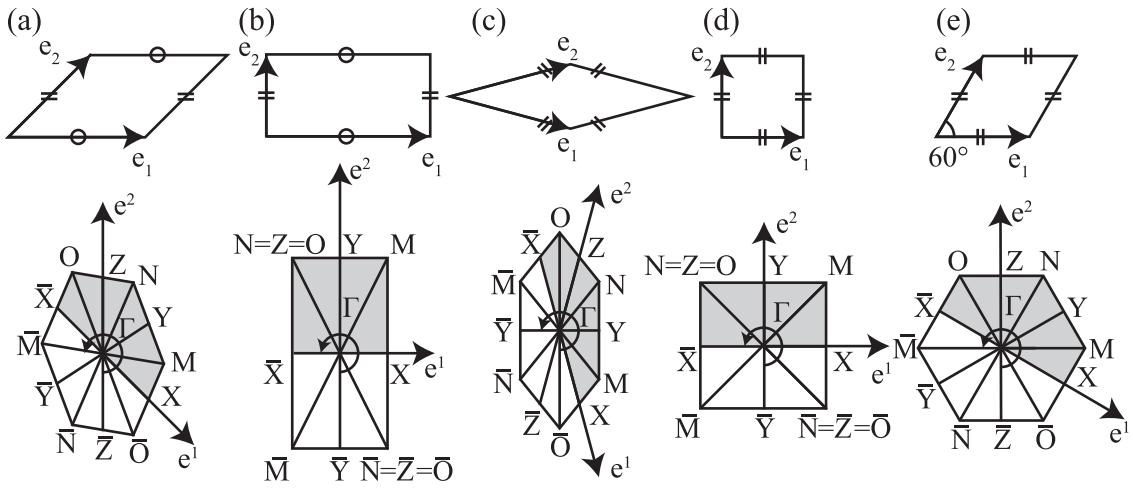


**Fig. 1.** The oblique (a), rectangular (b), rhombic (c), square (d), and hexagonal (e) unit cells with corresponding BZ. The symbol ↻ indicates that the IBZ in gray, corresponding to the groups *p1* or *p2*, can be arbitrarily rotated around the center Γ.

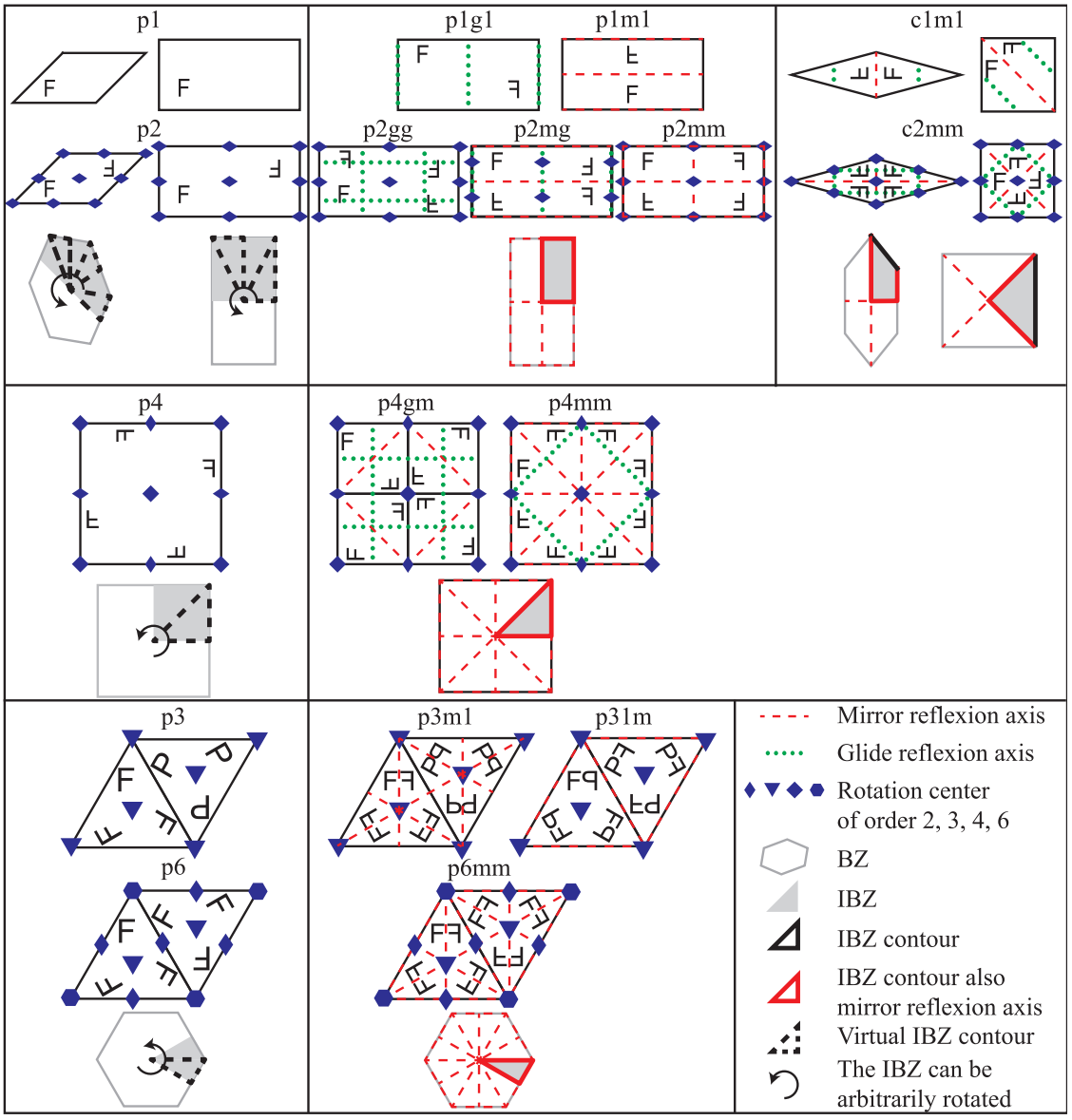


**Fig. 2.** BZ and IBZ for the 17 plane crystallographic groups. The Bravais lattices are given for the most general configurations, see Table 4 for all compatible ones. For sake of clarity, the direct and reciprocal basis vectors are omitted here, but are reported in Fig. 1. The glide reflection axes are also omitted for *p3m1, p31m*, and *p6mm*.

**Table 3**
The plane crystallographic group of a lattice in terms of its highest order of rotational symmetry and its reflection axis (Radaelli, 2011).

| Highest rotation? | Has mirrors? | | | |
|---|---|---|---|---|
| | Yes | | No | |
| 360°/6 | *p6mm* | | *p6* | |
| 360°/4 | Has mirrors at 45°? | | *p4* | |
| | Yes: *p4mm* | No: *p4gm* | | |
| 360°/3 | Has rotation centre off mirrors? | | *p3* | |
| | Yes: *p31m* | No: *p3m1* | | |
| 360°/2 | Has perpendicular mirrors? | | Has glide? | |
| | Yes | No | | |
| | Has rotation centre off mirrors? | *p2mg* | Yes: *p2gg* | No: *p2* |
| | Yes: *c2mm* / No: *p2mm* | | | |
| None | Has glide axis off mirrors? | | Has glide? | |
| | Yes: *c1m1* | No: *p1m1* | Yes: *p1g1* | No: *p1* |

**Table 4**
Plane crystallographic group (PCG), point group (PG), possible unit cell shape, IBZ definition and its contour, and BZ/IBZ size ratio $r$. $_d$ and $_r$ stands for the direct and reciprocal spaces, respectively.

| $PCG_d$ | $PG_d$ | Obl | Rec | Rho | Squ | Hex | $PCG_r$ | $PG_r$ | IBZ | IBZ contour | $r$ |
|---|---|---|---|---|---|---|---|---|---|---|---|
| *p1* | $C_1$ | ✓ | ✓ | ✓ | ✓ | ✓ | *p2* | $C_2$ | $\circlearrowleft \Gamma X M Y N Z O \bar{X} \Gamma$ | $\Gamma X M \Gamma Y N \Gamma Z O \Gamma$ | 2 |
| *p2* | $C_2$ | | | | | | | | | | |
| *p4* | $C_4$ | | | | ✓ | | *p4* | $C_4$ | $\circlearrowleft \Gamma X M Y \Gamma$ | $\Gamma X M \Gamma$ | 4 |
| *p1m1* | $D_1$ | | | | | | | | | | |
| *p1g1* | | | | | | | | | | | |
| *p2mm* | $D_2$ | | ✓ | | ✓ | | *p2mm* | $D_2$ | $\Gamma X M Y \Gamma$ | $\Gamma X M Y \Gamma$ | |
| *p2mg* | | | | | | | | | | | |
| *p2gg* | | | | | | | | | | | |
| *c1m1* | $D_1$ | | | ✓ | ✓ | | *c2mm* | $D_2$ | $\Gamma \bar{O} X M \Gamma$ | $\Gamma \bar{O} X M \Gamma$ | |
| *c2mm* | $D_2$ | | | | | | | | | | |
| *p3* | $C_3$ | | | | | ✓ | *p6* | $C_6$ | $\circlearrowleft \Gamma X M Y \Gamma$ | $\Gamma X M \Gamma$ | 6 |
| *p6* | $C_6$ | | | | | | | | | | |
| *p4mm* | $D_4$ | | | | ✓ | | *p4mm* | $D_4$ | $\Gamma X M \Gamma$ | $\Gamma X M \Gamma$ | 8 |
| *p4gm* | | | | | | | | | | | |
| *p3m1* | $D_3$ | | | | | ✓ | *p6mm* | $D_6$ | $\Gamma X M \Gamma$ | $\Gamma X M \Gamma$ | 12 |
| *p31m* | | | | | | | | | | | |
| *p6mm* | $D_6$ | | | | | | | | | | |

The point group of a two-dimensional unit cell is composed by two families, the cyclic point group denoted $C_n$, when only rotations are involved, and the dihedral point group, $D_n$, for which the unit cell possesses at least one mirror or glide reflection symmetry. The subscript $n$ indicates the highest order of the rotational symmetry (rotation by 360°/$n$).

The plane crystallographic group describes periodic lattices and is denoted by two or four characters for the cyclic and dihedral point group, respectively (Hahn, 2002; Grubaum and Shephard, 2013; Radaelli, 2011). If no mirror or glide reflection is present, the nomenclature is *pn* and is equivalent to $C_n$, except that *pn* is restricted to the description of periodic lattice. When mirror or glide reflections are present, the crystallographic denotation is *pnxy* or *cnxy*. The first letter "*p*" or "*c*" holds for a primitive or centered unit cell, respectively. The two last letters indicate symmetries relative to the main axis of the lattice (the main axis is arbitrarily chosen between the two translation axes, except if only one of them (being the main one) is perpendicular to a mirror axis). The letters "*x*" and "*y*" can take the values "m", "g", or "1", holding for mirror reflection, glide reflection, or none, respectively. Moreover, "*x*" indicates symmetry of axis perpendicular to the main axis whereas "*y*" indicates if the symmetry axis is parallel or tilted by 180°/$n$ with respect to the main axis. For instance, *p4gm* means that the lattice has 4-fold rotations, a glide reflection perpendicular to the main axis, and a mirror axis at 45°. Once the periodicity of the lattice is identified, Tables 3 and 4 and Fig. 2 can be used to determine the plane crystallographic group of the considered lattice.

Based on the work of Cracknell (1974) and assuming time-invariant media, the IBZ are illustrated for the 17 plane crystallographic groups in Fig. 2, and information on the IBZ are tabulated in Table 4.

For unit cells belonging to the cyclic groups, the corresponding BZ are also in the cyclic group. It means that the IBZ can be arbitrarily rotated around $\Gamma$ (no mirror symmetry) and this justify the presence of the symbol $\circlearrowleft$ on the BZ. Consequently, there is an infinite number of possible polygons for the IBZ, and two of them are illustrated in Fig. 3a. However, it is more convenient to use the IBZ for which the corners correspond to the points *X, M, Y, N* etc., and we arbitrary define the first side of the polygon by $\Gamma X$ for primitive unit cells and by $\Gamma \bar{O}$ for centered unit cells, the other corners of the polygon being defined in the counter clockwise direction.

The contour of the IBZ is now discussed. For the reciprocal space with mirror symmetries, the choice of IBZ is unique and the contour of the IBZ is defined as the boundaries of the IBZ. For the cyclic groups, since the IBZ can be arbitrarily rotated, the definition of the IBZ contour does not really exist (there is an infinite number of possible contour that covers the full BZ).

However, as the goal of the present paper is to provide probabilities of band-gap extrema to be on a given path, a contour is constructed artificially by considering the bisectors and the diagonals inside the IBZ. Taking advantage of the cyclic rotation and the translational periodicity of the BZ, some portions are found redundant, and a possible minimum path is highlighted in dashed black lines for each IBZ (see Figs. 2 and 3). This artificial path that does not correspond to any possible contour is refereed next as the

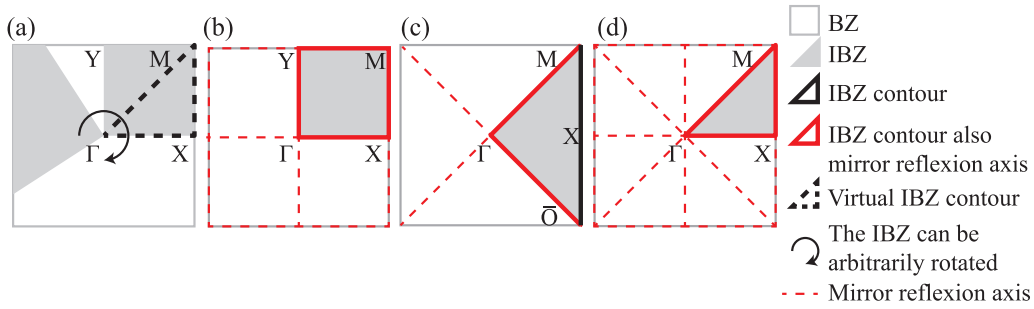


**Fig. 3.** BZ and IBZ for square unit cells with reciprocal space of symmetry *p4* (a), *p2mm* (b), *c2mm* (c), and *p4mm* (d). Note that in (a), the IBZ is not unique and can be arbitrarily rotated.

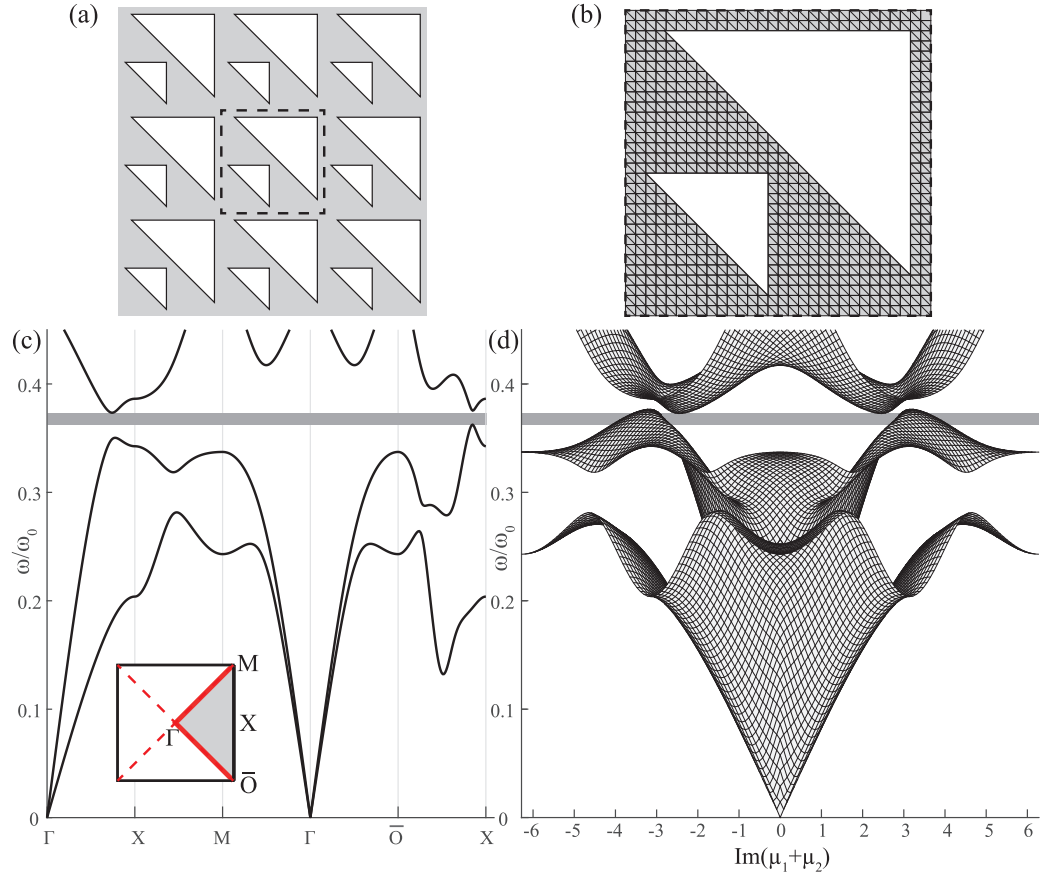


**Fig. 4.** Periodic Sierpinski right-angled isosceles triangles with a porosity of 40% (a), and a detailed discretized unit cell (b). Dispersion curves at the contour of the IBZ (c) and dispersion surfaces for the full BZ (d). The band-gap, in gray, is not omnidirectional.

virtual IBZ contour. For instance, in the reciprocal space of symmetry *p4*, if the square Γ*XMY*Γ is considered as the IBZ, the path following the contour and its diagonal is defined by the polyline Γ*XM*Γ*YM*Γ. However, the cyclic group of the BZ is $C_4$ meaning that the dispersion curves on the segment Γ*X* will be identical as the one on Γ*Y* (the following notation is introduced to denote this equality: $\omega_{\overrightarrow{\Gamma X}} = \omega_{\overrightarrow{\Gamma Y}}$). For the same reason, $\omega_{\overrightarrow{MY}} = \omega_{\overrightarrow{OX}}$, and due to the periodicity of the reciprocal space, $\omega_{\overrightarrow{OX}} = \omega_{\overrightarrow{MX}}$ such that one get $\omega_{\overrightarrow{MY}} = \omega_{\overrightarrow{MX}}$. Consequently, the virtual IBZ contour for the reciprocal space of symmetry *p4* is the polyline Γ*XM*Γ.

For those groups, the fact that the virtual contour differs from the IBZ boundary is a common source of confusion (see Table 1). For instance, for square unit cells, the group *p4* (Fig. 3a) the virtual contour is the same as the IBZ contour of the group *p4mm* (Fig. 3d), whereas the IBZ area is two times larger and can be the one of the group *p2mm* (Fig. 3b) or the group *c2mm* (Fig. 3c). Another common source of error for centered unit cells (e.g. Fig. 3c) is the fact that their IBZ orientations is shifted by 45° with respect to the ones of some primitive unit cells (e.g. Fig. 3b).

Now that the IBZ and its contour are defined, the goal of the next section is to see for the 17 lattices what are the consequences of restricting the band-gap analysis to the IBZ contour.

## 3. Band-gaps and IBZ contours

In the literature, the band-gap detection is often restricted to the IBZ contour, while it has been shown for the groups *p1* (Nojima and Kamakura, 2008; Harrison et al., 2007; Farzbod and Leamy, 2011), *p1m1* (Harrison et al., 2007), and *c1m1* (Gorshkov et al., 2017) that band-gap extrema can be located inside the IBZ. In this section, the probability of occurrence of such an event for each of the 17 plane crystallographic groups will be provided. But before, a

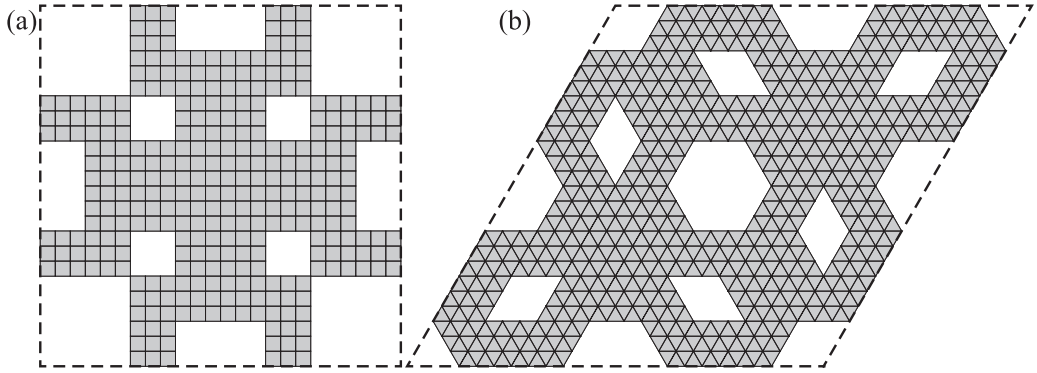


**Fig. 5.** Examples of a *p4mm* square (a) and a *p6mm* hexagonal (b) discretized unit cell.

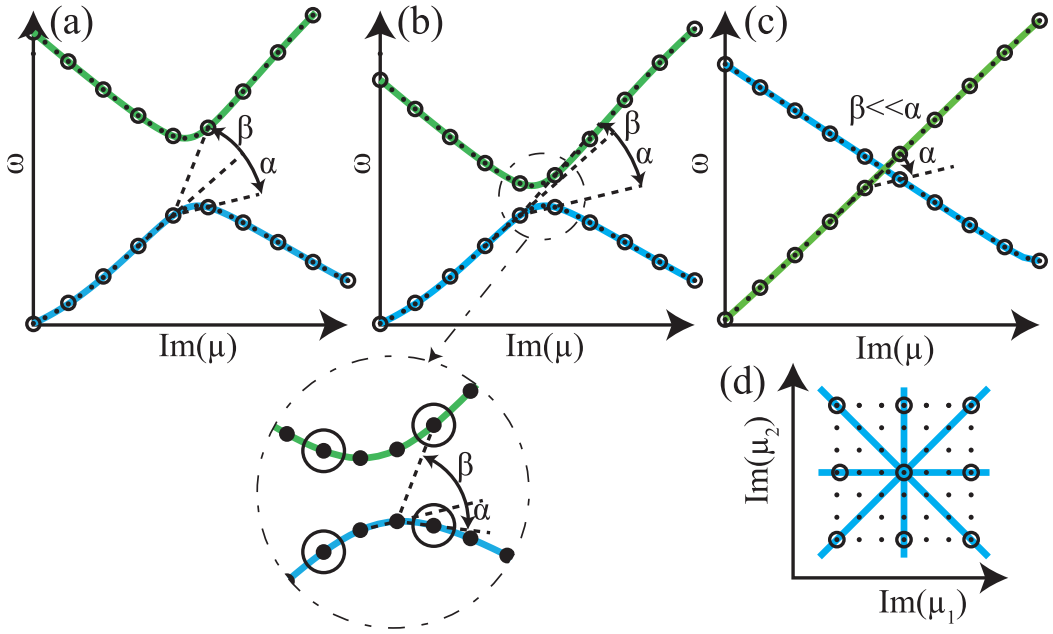


**Fig. 6.** Examples of a band-gap (a,b) and dispersion curves intersection (c). The large circles and small dots represent coarse and fine discretization of the wave vectors, respectively. For (b), the band-gap is detected with the fine discretization, but not with the coarsest one. For dispersion surfaces, the detection is done in the 4 directions (d).

structure already investigated in the literature is revisited, to show that the band-gaps observed on the IBZ contour are not always full. In this section, all numerical computations are performed using *Matlab*.

### 3.1. Band-gap present on the IBZ contour, but not full

In this example, the Sierpinski triangle fractal porous phononic crystal investigated in Wang et al. (2016a) is revisited. We focus on the case of the first fractal level of the right-angled isosceles triangle (Fig. 4a) with a porosity of 40%. The unit cell, of length $l = 0.02$ m, is divided into a grid of $30 \times 30$, and each pixel of this grid is divided into two right-angled isosceles triangle finite elements, as shown in Fig. 4b. As in Wang et al. (2016a), the pore are vacuum, and the plane strain matrix material is aluminum, of density $\rho = 2700$ kg m$^{-3}$, and first and second Lamé coefficient $\lambda = 68.3$ GPa and $\mu = 28.3$ GPa, respectively. The normalized frequency is $\omega_0 = 2\pi c_t/l$, where $c_t = \sqrt{E/\rho/2/(1+\nu)}$, $E = \mu(3\lambda + 2\mu)/(\mu + \lambda)$ and $\nu = \lambda/2/(\mu + \lambda)$.

The square unit cell has one of its diagonals mirror symmetric; the group is *c1m1*, and the IBZ is the triangle $\Gamma\bar{O}XM\Gamma$. The dispersion curves for this path are provided in Fig. 4c and a band-gap can be observed around $\omega/\omega_0 = 0.36$. However, when the dispersion surfaces over the full IBZ are considered (Fig. 4d), no full band-gap is obtained. The band-gap is not omnidirectional. This can be a problem experimentally, where a predicted wave attenuation will not be observed. The next part investigates the probability of occurrence of such an event for each plane crystallographic groups.

### 3.2. Band-gaps, IBZ contours and statistics

The goal of this part is to answer to the three following questions:

- For full band-gaps, what is the probability that an extremum is not located on the IBZ contour, but inside?
- When the analyses is restricted to the IBZ contour, what is the probability that the observed band-gap is not full?
- When the analyses is restricted to the IBZ contour, what is the averaged bandwidth error?

To give an answer to the questions raised above, the monomaterial phononic crystal used in the previous example is reconsidered, although the results might strongly depend on the physics (Bragg/resonance scattering, EM/ED waves...). The aim of this work is to highlight the differences on the above questions for the different symmetries.

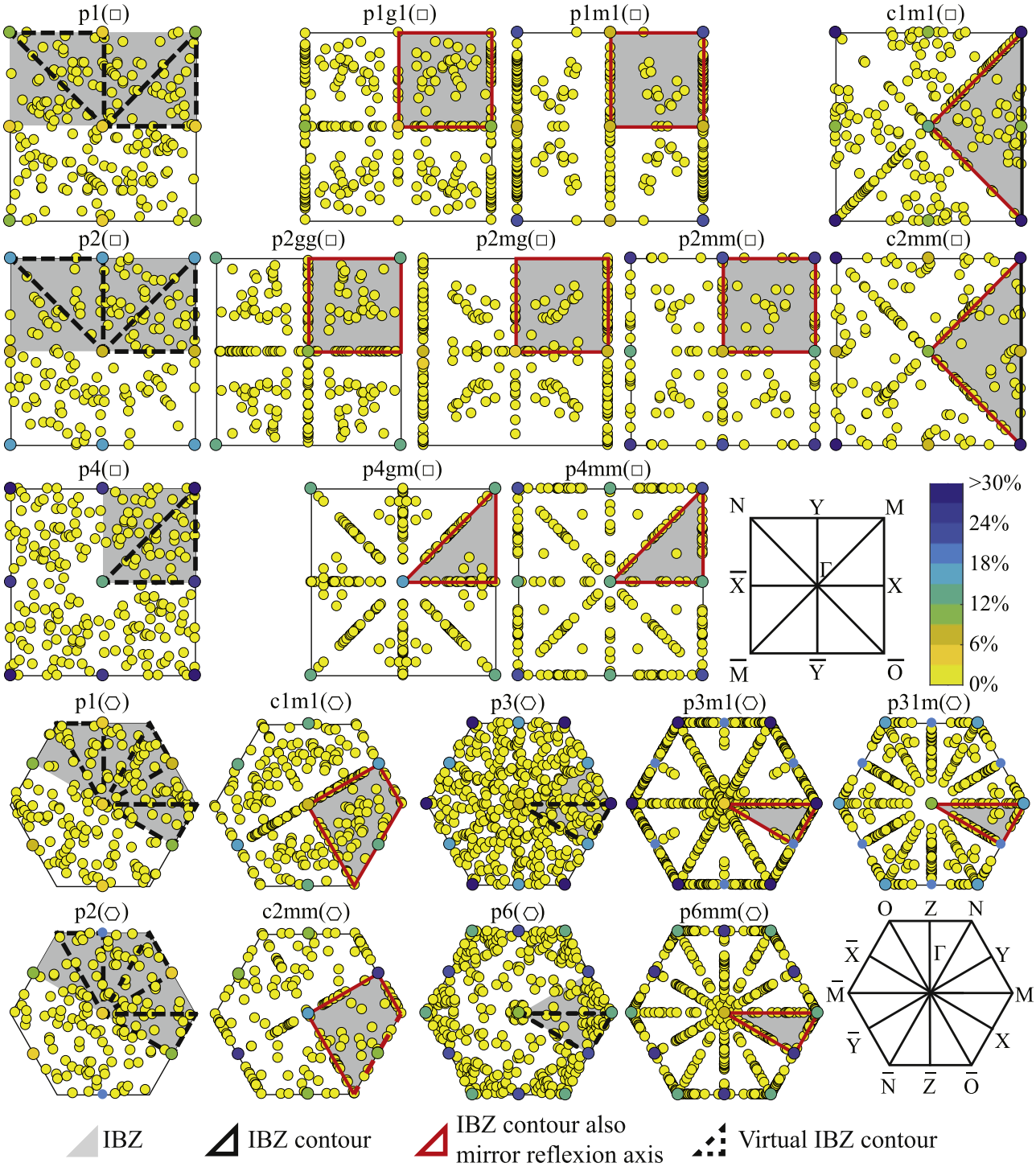


**Fig. 7.** Localization in the BZ of 300 randomly selected full band-gap extrema, for the different plane crystallographic groups possessing square (□) or hexagonal (⬡) BZ. The scale indicates the percentage of times a position of the IBZ is targeted.

*3.2.1. Problem description*

To get such statistics, hundreds of different geometries have to be simulated. To this end, two unit-cell types are considered; square and hexagonal ones, allowing to test the 17 symmetries (see two examples in Fig. 5). The square unit cell is modeled by a grid of size $n \times n$, where each pixel can take the value 0 (vacuum) or 1 (matter, presence of one element). This give $2^{(n^2)}$ possible combinations, but most of them are not valid. Indeed, the following constraints have to be respected:

- All the elements should form a single group. Two elements are considered grouped if they share an edge. Note that connections at the corner are considered in the physical model (see an example in Fig. 5a), but are not accounted for when detecting the groups to avoid freely rotating elements.
- To fulfil the periodic boundary conditions, the matter should join each edge of the unit cell. Moreover, there should be at least one element by edge mirror symmetric with its opposite edge.

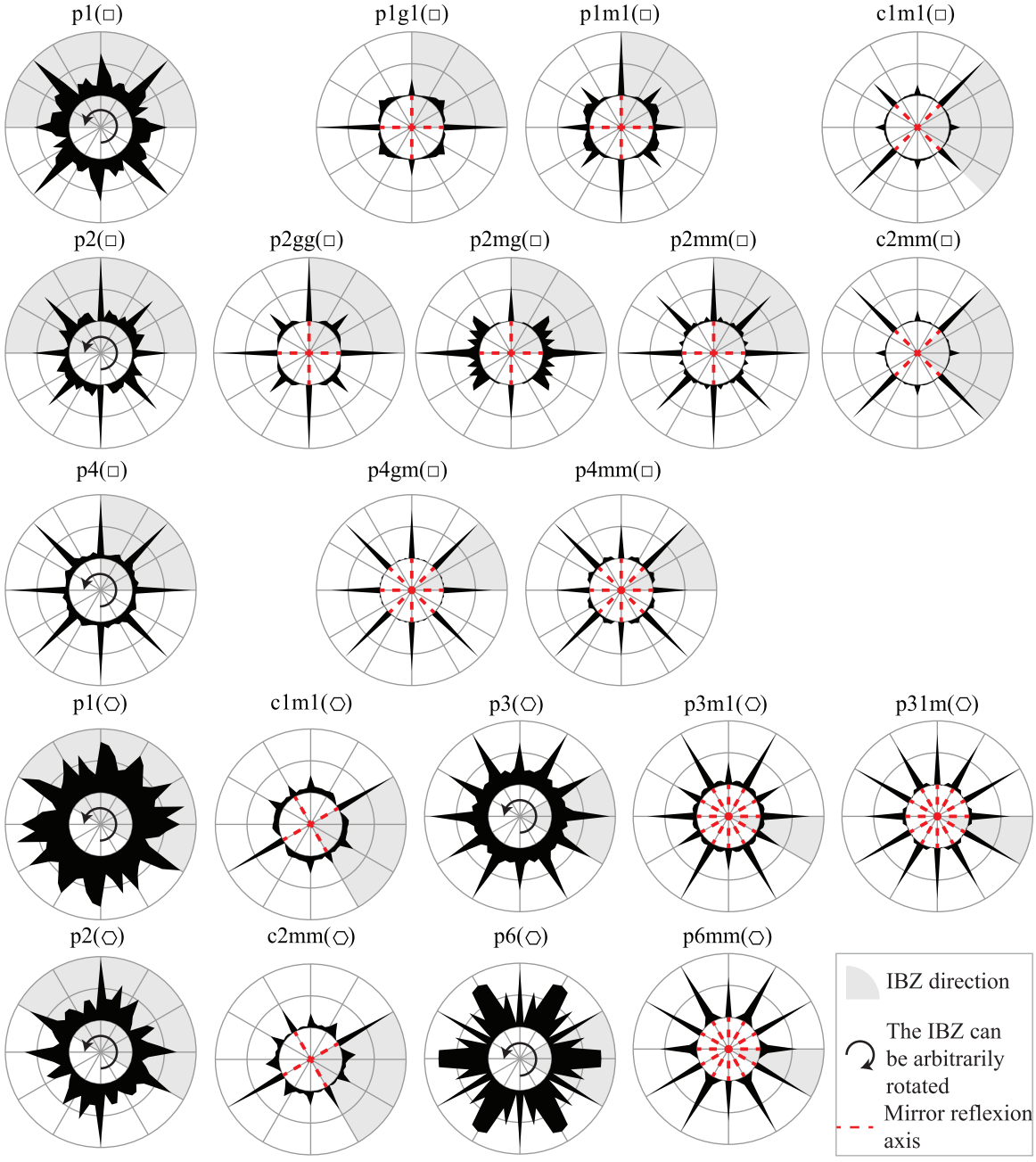


**Fig. 8.** Averaged orientation of the full band-gaps extrema, for the different plane crystallographic groups possessing square (□) or hexagonal (⬡) BZ.

- The unit cell has to respect the desired symmetry group: it is necessary to check that the unit cell is the minimum one, and that there are no higher symmetries embedded in the unit cell. For example, for a *p2mm* pattern, the bisectors are mirror axes, but if the diagonals are also mirror axes, the resulting group is *p4mm*.

For a grid of $8 \times 8$, there are $1.8 \times 10^{19}$ possible combinations, but the configurations that fulfil the above requirements are too few to be detected in a reasonable computational time. In order to reduce the number of grids to be tested, the symmetry is imposed first. This is possible for all the groups except for *p1* (no symmetry to be imposed), for which the grid is reduced to $6 \times 6$. At the end, there are 150 possible grids having the group *p4mm*, whereas for the other symmetries, a subset of around 200 different geometries is selected. Note that the subset is not composed by the 200 first grids, but the selected patterns are spread among all valid combinations. Indeed, in the way we implement it, only one pixel changes between two consecutive combinations such that a subset formed by consecutive combinations would not be representative.

For hexagonal unit cells, the idea is strictly identical, except that the grid is sheared and inclined by an angle of $\pi/3$, and each element is cut in two, resulting to an equilateral triangular mesh. The grid is $8 \times 8$ for *p2, c1m1, c2mm* and *p6mm*, whereas it is $6 \times 6$ for *p1, p3, p6, p3m1* and *p31m*.

For a given pattern, each element is then split into 9 (3 by directions) to generate smaller finite elements. Indeed, the mesh size $h$ has to be smaller than 1/8 of the minimum wavelength. Consequently, the considered frequencies are smaller than $w_{\max} = w_0 L/8/h$.

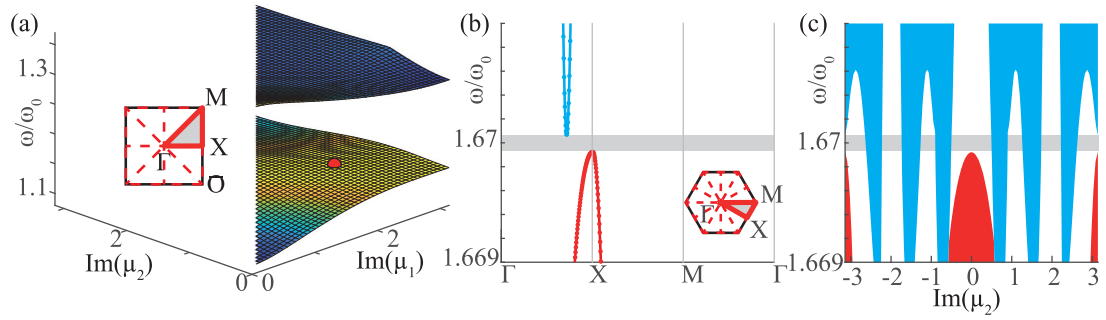


**Fig. 9.** (a) Fifteenth and sixteenth dispersion surfaces in the IBZ for the unit cell presented in Fig. 5a. Note that a full band-gap is present between both bands, with the maximum of the fifteenth band (circle marker) inside the IBZ. Fifteenth and sixteenth dispersion curves around the IBZ (b) and dispersion bands in the BZ (c) for the unit cell presented in Fig. 5b. Note that the band-gap in gray (b) is not full (c).

When discrete dispersion curves or surfaces are obtained, one should distinguish between band-gaps and curve/surface intersections. Given two dispersion curves, the angles $\alpha$ and $\beta$ are computed at a given discrete wavenumber as illustrated in Fig. 6. If $\alpha > \beta$, the curves are intersecting (Fig. 6c). A band-gap is present if $\alpha < \beta$ for all the discrete points of the curve (Fig. 6a). Moreover, the second derivative of the point before in the lower band has to be negative, whereas the second derivative of the point after in the upper band has to be positive. Using this method, some band-gaps can be miss-detected, as shown in Fig. 6b, but the quality of the detection improves when the discretization is refined (see zoomed area). A balance between the quality of the results, and the computation time has to be find. In the present work, the two reciprocal vectors are both discretized by 120 steps, and it has been checked visually for a sample of simulations that the detection is properly processed. Band-gaps between two surfaces are detected by investigating band-gaps between two curves along four directions, as illustrated in Fig. 6d. Note that the proposed method does not guaranty that some curves intersect in some other directions, but better solutions are unknown to the author's knowledge. Nevertheless, this method seems to work while inspecting some dispersion bands.

**Table 5**
For the 17 plane crystallographic groups (PCG) with square (□) and hexagonal (⬡) unit cells, statistics of the band-gap (BG) localizations, probabilities to get non-full band-gaps, and averages of the bandwidth (BW) error made when only the IBZ contour is considered.

| | For full BG, | If restricted to IBZ contour, % of | |
|---|---|---|---|
| PCG | % on IBZ contour | non-full BG | the BW error |
| *p1* (□/⬡) | 23.75/30.85 | 38.26/29.84 | 62.01/46.83 |
| *p2* (□/⬡) | 40.60/41.86 | 62.80/62.93 | 71.52/68.53 |
| *p4* (□) | 66.11 | 41.90 | 47.02 |
| *p1m1* (□) | 90.93 | 4.11 | 8.26 |
| *p1g1* (□) | 76.45 | 5.49 | 14.30 |
| *p2mm* (□) | 94.46 | 8.71 | 9.99 |
| *p2mg* (□) | 87.05 | 31.19 | 33.94 |
| *p2gg* (□) | 85.50 | 24.19 | 27.67 |
| *c1m1* (□/⬡) | 84.28/81.98 | 4.01/6.52 | 9.24/10.78 |
| *c2mm* (□/⬡) | 91.07/91.80 | 17.16/12.07 | 18.41/13.18 |
| *p3* (⬡) | 59.36 | 7.44 | 16.11 |
| *p6* (⬡) | 61.42 | 38.94 | 44.26 |
| *p4mm* (□) | 99.43 | 3.30 | 3.30 |
| *p4gm* (□) | 97.86 | 2.09 | 2.70 |
| *p3m1* (⬡) | 99.69 | 3.65 | 3.65 |
| *p31m* (⬡) | 99.21 | 0.26 | 0.30 |
| *p6mm* (⬡) | 100.00 | 0.42 | 0.42 |

### 3.2.2. Results

When full band-gaps are present, positions of the extrema relative to the BZ are plotted in Fig. 7, for the plane crystallographic groups possessing square and hexagonal BZ. The first overall observation is that the extrema are more located on the mirror axes of the BZ, if present (no mirror axis for the cyclic group). Moreover, the more there are reflection axes, the less extrema are inside the IBZ. However, there are some portions of the IBZ contour for which the probability is low:

- For the two groups possessing centered square unit cells (*c1m1, c2mm*), almost no extrema are located on the segments composing the BZ contour (e.g. $]XM[$ or $]X\bar{O}[$). It is explained by the fact that these axes are not mirror axes. Consequently, when the analysis is restricted to the IBZ contour, these portions can be avoided. However, the probability at the middle of the edges (i.e. $X$) is important, and since the band-gap detection cannot be operated from a single point, at least one segment should be kept.
- For the groups *p1g1, p1m1, p2gg, p2mg, p2mm* and *p4mg*, some portions of the BZ contour are without extrema, but we don't have proper explanations for these cases.

As a consequence of the absence of extremum at some portions of the IBZ contour, the band-gaps are more present in some directions. This is highlighted by the polar plots of the band-gap orientations provided in Fig. 8. For instance *p4gm* will be more directional than *p4mm*. As also expected, when the lattice has no mirror axis, all the directions are targeted even if some peaks are present at multiples of 45° for the square unit cells and 30° for the hexagonal ones. Indeed, several band-gaps can share a same location (see the color scale of Fig. 7), being especially true at the positions indicated by letters (e.g. $\Gamma$, $X$, $M$). If one is looking for a unit cell with some required band-gap directions, these wind roses can be used to fix the unit cell symmetry at an early stage of the design process.

The probability that a full band-gap extremum is located on the contour is given in Table 5 (although it has been shown that some portions of the IBZ have a really low probability to have extrema, both real or virtual full contours are considered, for conservative reasons). It is found that this probability increases with the symmetry order of the lattice, in agreement with the previous observations. However, contrary to what is often stated in the literature, for the fully symmetric square unit cell *p4mm*, the probability is not 100% (see the point in the middle of the IBZ in Fig. 7). The unit cell design resulting to this result is shown in Fig. 5a and details on the dispersion surfaces are shown in Fig. 9a. For *p6mm*, considering our simulations, the probability is 100%. This does not guaranty the nonexistence of contradictory examples, but it can be said that for this group, the band-gap extrema are located on the IBZ contour.

Based on these results, one could think that restricting to the contour to retrieve band-gaps is sufficient, but this does not mean that the band-gaps are full. Indeed, the probability of occurrence of such an event is not null, even for the case *p6mm*, as also shown

in Table 5. This non-null percentage results from one unit cell design shown in Fig. 5b and for which, the dispersion curve and surfaces are shown in Fig. 9b and c. In conclusion, even with highly-symmetric porous phononic crystals, when looking for band-gaps, one can first consider the contour to see if band-gaps are possible, but then, the omnidirectionality has to be confirmed considering the full IBZ as proceeded for instance in Bacigalupo et al. (2017).

Finally, when the analysis is restricted to the IBZ contour, the bandwidth relative error is given by

$$\epsilon = \frac{BW_{\text{IBZcont}} - BW_{\text{IBZ}}}{BW_{\text{IBZcont}}}, \tag{3}$$

where the band-gap bandwidth measured on the IBZ contour and the one from the full surface are denoted by $BW_{\text{IBZcont}}$ and $BW_{\text{IBZ}}$, respectively. From this equation, if a band-gap extremum is located on the IBZ contour, the error will be 0% whereas if the band-gap is not full, the error will be 100%. Band-gap extrema located inside the IBZ will result to intermediate values. It is found that the bandwidth relative error is slightly larger than the percentage of non-full band-gaps, meaning that when restricting the analysis to the IBZ contour, the main error will be induced by the detection of non-full band-gaps.

As a last comment, for a crystallographic group having both a square and a hexagonal representations, their respective probabilities are close, meaning that the results are not so influenced by the geometry, but more by its symmetries.

## 4. Conclusions

When investigating periodic structures, it is primordial to know the crystallographic group of the considered unit cell, and the first part of this manuscript reviews how to identify it. The group symmetry of a lattice provides the IBZ, avoiding the analysis over the full BZ. The second part of the manuscript gives indications on the consequences of restricting the analysis to the IBZ contour. If the lattice possesses only rotational symmetries, without any reflection axis, the probability that extrema are not located on the contour or that the band-gaps are not full is high. This probability decreases with the number of reflection axes added, and relative good results can be obtained for the fully symmetric square or hexagonal unit cells. Although this can be sufficient at an early stage of the design process, it does not provided a full guaranty that a band-gap is full or located on the IBZ contour. Consequently, one can use the IBZ contour to pre-detect band-gaps, but their omnidirectionalities have to be confirmed considering the full IBZ.

While this work has been conducted for porous phononic crystals, statistics for different physics would deserve additional investigations.

## Acknowledgments

The Research Fund KU Leuven is gratefully acknowledged for its support. The research of F. Maurin is funded by an Experienced Researcher grant within the European ANTARES Project, under the FP7 Marie Curie Programme (GA606817). The European Commission also supports the research of C. Claeys through the ENLIGHT-project (GA314567). The research of E. Deckers is funded by a grant from the Research Foundation - Flanders (FWO).

## References

Ahmed, A., Alkhader, M., Abu-Nabah, B., 2017. In-plane elastic wave propagation in aluminum honeycomb cores fabricated by bonding corrugated sheets. J. Sandwich Struct. Mater.. 109963621772956.
Andreassen, E., Manktelow, K., Ruzzene, M., 2015. Directional bending wave propagation in periodically perforated plates. J. Sound Vib. 335, 187–203.
Bacigalupo, A., Gambarotta, L., 2016. Simplified modelling of chiral lattice materials with local resonators. Int. J. Solids Struct. 83, 126–141.
Bacigalupo, A., Gnecco, G., Lepidi, M., Gambarotta, L., 2017. Optimal design of low-frequency band gaps in anti-tetrachiral lattice meta-materials. Compos. Part B 115, 341–359.
Baravelli, E., Ruzzene, M., 2013. Internally resonating lattices for bandgap generation and low-frequency vibration control. J. Sound Vib. 332 (25), 6562–6579.
Bigoni, D., Guenneau, S., Movchan, A.B., Brun, M., 2013. Elastic metamaterials with inertial locally resonant structures: application to lensing and localization. Phys. Rev. B 87 (174303).
Brillouin, L., 1946. Wave Propagation in Periodic Structures; Electric Filters and Crystal Lattices. Courier Dover Publications.
C.-L.Yang, Zhao, S.-D., Wang, Y.-S., 2017. Experimental evidence of large complete bandgaps in zig-zag lattice structures.
Casadei, F., Rimoli, J., 2013. Anisotropy-induced broadband stress wave steering in periodic lattices. Int. J. Solids Struct. 50 (9), 1402–1414.
Celli, P., Gonella, S., 2015. Tunable directivity in metamaterials with reconfigurable cell symmetry. Appl. Phys. Lett. 106. 091905
Chen, Q., Elbanna, A., 2016. Modulating elastic band gap structure in layered soft composites using sacrificial interfaces. J. Appl. Mech. 83 (111009).
Claeys, C., Deckers, E., Pluymers, B., Desmet, W., 2016. A lightweight vibro-acoustic metamaterial demonstrator: numerical and experimental investigation. Mech. Syst. Signal Process. 70–71, 853–880.
Collet, M., Ouisse, M., Ruzzene, M., Ichchou, M.N., 2011. Floquet-bloch decomposition for the computation of dispersion of two-dimensional periodic, damped mechanical systems. Int. J. Solids Struct. 48, 2837–2848.
Cracknell, A., 1974. Tables of the irreducible representations of the 17 two-dimensional space groups and their relevance to quantum mechanical eigenstates for surfaces and thin films. Thin Solid Films 21, 107–127.
Craster, R.V., Antonakakis, T., Makwana, M., Guenneau, S., 2012. Dangers of using the edges of the Brillouin zone. Phys. Rev. B 86 (115130).
Farzbod, F., Leamy, M.J., 2011. Analysis of Bloch's method and the propagation technique in periodic structures. J. Vib. Acoust. 133 (3), 031010.
Gao, N., Wu, J.H., Yu, L., Hou, H., 2016. Ultralow frequency acoustic bandgap and vibration energy recovery in tetragonal folding beam phononic crystal. Int. J. Modern Phys. B 30 (1650111).
Gonella, S., Ruzzene, M., 2008. Analysis of in-plane wave propagation in hexagonal and re-entrant lattices. J. Sound Vib. 312 (1), 125–139.
Gorshkov, V., Navadeh, N., Sareh, P., Tereshchuk, V., Fallah, A., 2017. Sonic metamaterials: reflection on the role of topology on dispersion surface morphology. Mater. Des..
Grubaum, B., Shephard, G.C., 2013. Tilings and Patterns. Dover Publications.
H.-W.Dong, Su, X.-X., Wang, Y.-S., Zhang, C., 2014. Topology optimization of two-dimensional asymmetrical phononic crystals.
Hahn, T., 2002. International Tables for Crystallography Volume A: Space-Group Symmetry. Kluwer.
Harrison, J.M., Kuchment, P., Sobolev, A., Winn, B., 2007. On occurrence of spectral edges for periodic operators inside the brillouin zone. J. Phys. A 40, 7597–7618.
Hedayatrasa, S., Abhary, K., Uddin, M.S., Guest, J.K., 2016. Optimal design of tunable phononic bandgap plates under equibiaxial stretch. Smart Mater. Struct. 25, 055025.
Hladky-Hennion, A., Vasseur, J., Dubus, B., Djafari-Rouhani, B., Ekeom, D., Morvan, B., 2008. Numerical analysis of negative refraction of transverse waves in an elastic material. J. Appl. Phys. 104, 064906.
Huang, J., Ruzzene, M., Chen, S., 2017. Analysis of in-plane wave propagation in periodic structures with Sierpinski-carpet unit cells. J. Sound Vib. 395, 127–141.
Kittel, C., 2007. Introduction to Solid State Physics, 2004. Wiley.
Lardeau, A., Groby, J.-P., Romero-García, V., 2016. Broadband transmission loss using the overlap of resonances in 3d sonic crystals. Crystals 6 (51).
Li, Y., Chen, T., Wang, X., Yu, K., Song, R., 2015. Band structures in two-dimensional phononic crystals with periodic jerusalem cross slot. Physica B 456, 261–266.
Liu, J., Li, L., Xia, B., Man, X., 2017. Fractal labyrinthine acoustic metamaterial in planar lattices. Int. J. Solids Struct..
Liu, X., Hu, G., Sun, C., Huang, G., 2011. Wave propagation characterization and design of two-dimensional elastic chiral metacomposite. J. Sound Vib. 330 (11), 2536–2553.
Liu, Y., Su, J.-Y., Xu, Y.-L., Zhang, X.-C., 2009. The influence of pore shapes on the band structures in phononic crystals with periodic distributed void pores. Ultrasonics 49 (2), 276–280.
Maurin, F., 2016. Bloch theorem with revised boundary conditions applied to glide and screw symmetric, quasi-one-dimensional structures. Wave Motion 61, 20–39.
Maurin, F., Claeys, C., Belle, L.V., Desmet, W., 2017. Bloch theorem with revised boundary conditions applied to glide, screw and rotational symmetric structures. Comput. Methods Appl. Mech. Eng. 318, 497–513.
Meng, F., Li, Y., Li, S., Lin, H., Jia, B., Huang, X., 2017. Achieving large band gaps in 2d symmetric and asymmetric photonic crystals. J. Lightwave Technol. 35, 1670–1676.
Miniaci, M., Krushynska, A., Movchan, A., 2016. Spider web-inspired acoustic metamaterials. Appl. Phys. Lett..
Nojima, S., Kamakura, Y., 2008. Irreducible first Brillouin-zone for two-dimensional binary-compound photonic crystals. J. Phys. Soc. Jpn. 77 (034403).
Palermo, A., Marzani, A., 2016. Extended bloch mode synthesis: ultrafast method for the computation of complex band structures in phononic media. Int. J. Solids Struct. 100, 29–40.
Phani, A.S., Woodhouse, J., Fleck, N.A., 2006. Wave propagation in two-dimensional periodic lattices. J. Acoust. Soc. Am. 119 (4), 1995–2005.

Piccolroaz, A., Movchan, A., Cabras, L., 2017. Rotational inertia interface in a dynamic lattice of flexural beams. Int. J. Solids Struct. 112, 43–53.
Radaelli, P.G., 2011. Symmetry in Crystallography : Understanding the International Tables. Oxford University Press.
Reda, H., Ganghoffer, J., Lakiss, H., 2017. Micropolar dissipative models for the analysis of 2d dispersive waves in periodic lattices. J. Sound Vib. 392, 325–345.
Schaeffer, M., Ruzzene, M., 2015. Wave propagation in reconfigurable magneto-elastic kagome lattice structures. J. Appl. Phys. 117, 194903.
Shim, J., Wang, P., Bertoldi, K., 2015. Harnessing instability-induced pattern transformation to design tunable phononic crystals. Int. J. Solids Struct. 58, 52–61.
Shmueli, U., 2008. International Tables for Crystallography, Volume B: Reciprocal Space. Springer, Netherlands.
Spadoni, A., Ruzzene, M., Cunefare, K., 2009. Vibration and wave propagation control of plates with periodic arrays of shunted piezoelectric patches. J. Intell. Mater. Syst. Struct. 20, 979–990.
Spadoni, A., Ruzzene, M., Gonella, S., Scarpa, F., 2009. Phononic properties of hexagonal chiral lattices. Wave Motion 46 (7), 435–450.
Tallarico, D., Movchan, N.V., Movchan, A.B., Colquitt, D.J., 2017. Tilted resonators in a triangular elastic lattice: chirality, Bloch waves and negative refraction. J. Mech. Phys. Solids 103, 236–256.
Trainiti, G., Rimoli, J., Ruzzene, M., 2016. Wave propagation in undulated structural lattices. Int. J. Solids Struct. 97, 431–444.
Wang, K., Liu, Y., Liang, T., 2016. Band structures in Sierpinski triangle fractal porous phononic crystals. Physica B 498, 33–42.
Wang, P., Casadei, F., Shan, S., Weaver, J.C., Bertoldi, K., 2014. Harnessing buckling to design tunable locally resonant acoustic metamaterials. Phys. Rev. Lett. 113 (014301).
Wang, T., Sheng, M.-p., Wang, H., Qin, Q.-H., 2015. Band structures in two-dimensional phononic crystals with periodic s-shaped slot. p6 43, 275–281.
Wang, Z., Zhang, Q., Zhang, K., Hu, G., 2016. Tunable digital metamaterial for broadband vibration isolation at low frequency. Adv. Mater. 28, 9857–9861.
Yilmaz, C., Hulbert, G.M., Kikuchi, N., 2007. Phononic band gaps induced by inertial amplification in periodic media. Phys. Rev. B 76, 054309.
Zhao, S.-D., Wang, Y.-S., 2016. Negative refraction and imaging of acoustic waves in a two-dimensional square chiral lattice structure. C.R. Phys. 17 (5), 533–542.
Zhu, R., Liu, X.N., Hu, G.K., Sun, C.T., Huang, G.L., 2014. Negative refraction of elastic waves at the deep-subwavelength scale in a single-phase metamaterial. Nat. Commun. 5 (5510).
Zhu, Z., Deng, Z., 2016. Tailoring of interiorly resonant band gaps in structurally square re-entrant honeycombs. J. Sound Vib. 372, 181–191.

# Update

International Journal of Solids and Structures
Volume 193–194, Issue , 1 June 2020, Page 502

DOI: https://doi.org/10.1016/j.ijsolstr.2020.01.013

International Journal of Solids and Structures 193–194 (2020) 502

Contents lists available at ScienceDirect

International Journal of Solids and Structures

journal homepage: www.elsevier.com/locate/ijsolstr

Corrigendum

# Corrigendum to "Probability that a band-gap extremum is located on the irreducible Brillouin-zone contour for the 17 different plane crystallographic lattices" [International Journal of Solids and Structures, 135 (2018) 26–36]

Florian Maurin[a,b,*], Claus Claeys[a,b], Elke Deckers[a,b], Wim Desmet[a,b]

[a] KU Leuven, Department of Mechanical Engineering, Division PMA Celestijnenlaan 300, Leuven B-3001, Belgium
[b] Flanders Make, Belgium

The authors regret to have wrongly defined in their code the input to generate figure 4. The consequence is that the dispersion curves provided in figure 4 does not correspond to the contour for which they are stated. This does not affect the rest of the manuscript and its conclusions.

The authors would like to apologise for any inconvenience caused.

DOI of original article: 10.1016/j.ijsolstr.2017.11.006
* Corresponding author.
*E-mail address:* florian.maurin@kuleuven.be (F. Maurin).

https://doi.org/10.1016/j.ijsolstr.2020.01.013